International Conference on Space Optics—ICSO 1997

Toulouse, France

2–4 December 1997

Edited by George Otrio

A demonstrator for an incoherent Doppler wind lidar receiver

F. Fabre, A. Marini, Thomas C. Sidler, Didier Morancais, et al.

International Conference on Space Optics — ICSO 1997, edited by Georges Otrio, Proc. of SPIE Vol. 10570, 1057005 · © 1997 ESA and CNES · CCC code: 0277-786X/18/$18 · doi: 10.1117/12.2326433

A Demonstrator for an Incoherent Doppler Wind Lidar receiver.

F. FABRE[1], A. MARINI[2], Th. SIDLER[3], D. MORANCAIS[1], G. FONGY[1], Ph. VIDAL[1],

(1) :MATRA-MARCONI-SPACE, 31, rue des Cosmonautes - 31 402 Toulouse Cedex 4 - France

(2): ESA-ESTEC : Keplerlaan, 1 2200 AG Noordwijk - The Netherlands

(3): Ecole Polytechnique Fédérale de Lausanne , CH-ECUBLENS - P.O Box 127 1015 Lausanne - Switzerland.

Abstract.

The knowledge of wind fields for a global terrestrial coverage and accurate altitude sampling is one of the main keys for improvement of meteorological predictions and general understanding of atmosphere behaviour. The best way to recover this information is remote sensing from space using low Earth orbit satellites. The measurement principle is to analyse the Doppler shift of the flux emitted by the space instrument and backscattered by the atmosphere. One of the most promising principle for Doppler shift measurement is the direct detection which does not need local oscillators, what significantly simplifies the design of such a space-borne receiver. ESA-ESTEC initiated at early 95' a programme called "Incoherent Doppler Wind Lidar (IDWL) technologies" for the study and bread-boarding phase. MMS won this contract proposing an original concept based on the use of a Fizeau high resolution interferometer working in the UV band, coupled with an intensified CCD. This concept is patented by MMS, as well as the special CCD timing sequence that will be depicted below. The programme begun by a study of the space-borne instrument in order to identify main constraints and define the receiver as could be for a flight model. A detailed performance model was established and parametric analysis allowed to optimise the concept in order to reach required performances. This study phase finally provided the definition of a bread-board for expected performances demonstration. Moreover, the Laser Signal Simulator (LSS) which is used to simulate the Lidar echo in term of amplitude as well as frequency modulation was defined at this step. The performances of this test support equipment are of main importance for the validation of the demonstrator design and performances. The second part of the study aimed at defining the detailed design of the demonstrator and associated test support equipments, as well as initiating preliminary validation experiments on most critical technologies, like Fizeau interferometer which needs particularly high thermal stability and spectral resolution. At the end of this design phase, the test bench equipments begun to be manufactured and equipment test results preliminary assessed the study phase results. After integration, the correct operation and control of the overall test bench were assessed and performance tests were undertaken . The final conclusion of this programme aimed at up-dating the performance simulation software in order to refine expected performances for the future flight instrument.

1. Introduction

The availability of wind fields measurements with global coverage and with high vertical resolution will play a key-role in extending the validity of numerical weather predictions and, more generally, in improving our understanding of the Earth atmosphere dynamics. It is now widely recognised that such measurements would be best provided by a satellite-observation system based on a space-borne Doppler wind lidar, sensing the atmosphere from the Low Earth Orbit [1]. The principle of the measurement consists in probing the atmosphere with laser pulses and analysing the Doppler shift of the radiation, backscattered by the atmosphere, which contains the actual information on the wind velocity. A promising technique for the measurement of the Doppler shift is the direct detection technique, which relies on a simplified instrument concept and receiver design. The European Space Agency (ESA) has initiated in early 95' a study called "Incoherent Doppler Wind Lidar (IDWL) technologies" for the definition and experimental validation of a Doppler wind lidar detection package, based on a direct detection technique. The study was awarded to MMS, which proposed an original concept based on the use of a high-resolution Fizeau interferometer, operating at UV wavelength, coupled with an intensified CCD. The work programme begun with a system analysis during which the mission requirements were taken into account, in order to preliminary establish the instrument design. These parameters, which are shown in table 1/1, were used to study different possible receiver configurations. The

Item	Proposed Requirements
P/F Altitude	520 km
LOS angle versus Nadir	33 °
Wavelength	355 nm
Vertical resolution	1 km
Cluster area	< 35 * 35 km
LOS measurement per cluster	1
Altitude range	0 to 30 km
Velocity dynamic range : . 0 to 10 km . 10 to 30 km	 ± 50 m/s ± 100 m/s
Measurement accuracy on horizontal winds .0 to 10 km . 10 to 30 km	 2 m/s (rms) 5 m/s (rms)
Bad measurement rate	< 20 %
Operation	Day and Night

Table 1/1 : *Summary of mission requirement*

instrument measures the horizontal wind with, at least, one Line Of Sight (LOS) measurement in a 200 x 200 km² horizontal cell. This is achieved by using a step-scanning concept, proposed during the previous ESA-funded ALADIN study [2]. The requirements for the instrument design are summarised in table 1.2.

Item	Hypothesis
Instrument mass	< 500 kg
Instrument Power	< 1 kW
Emitted optical power	15 W (0.15 J at 100 Hz)
Receiver useful diameter	700 mm
Emitter type	tripled Nd:Yag (355 nm)
Emitter pulse length	20 ns
Atmosphere model	ARMA (Atlid model extrapolated at 355 nm)

Table 1.2 : *Instrument design requirements*

The mass and power requirements are consistent with the spacecraft resources allocated for the mentioned ALADIN mission study and the emitted laser energy is selected in agreement with the state-of-the-art technology for diode-pumped solid-state lasers.

Two main types of direct receivers may be envisaged : receivers working on the Rayleigh backscattered signal (air molecules) or the Mie scattering (aerosols). The Rayleigh backscattered signal is spread over an optical bandwidth of about 0.6 pm while the Mie spectrum is essentially the same of the emitted laser pulse (0.02 pm). Since the theoretical accuracy on frequency measurement is proportional to the received signal spectrum, it appears that Mie receivers are much more accurate than Rayleigh one, for a given input signal. Nevertheless the performance of the receiver is dictated by the amount of backscatter return. The Mie signal rapidly decreases with altitude in the atmosphere, following the altitude dependence of aerosol concentration, while the Rayleigh signal remains rather constant, thanks to the uniform molecular distribution versus height. This means that the most interesting receiver could be made of a Mie channel for high accuracy at low altitude (0-6 km) and a Rayleigh channel for higher altitude with lower accuracy. Hovemere (UK) and CNRS (F), which were involved as consultants during the study phase, confirmed this approach by their respective study on Rayleigh and Mie receivers. At the end of the study phase, the Mie receiver was chosen to be bread-boarded since, on one hand, it provides better performances and, on the other hand, its feasibility is more critical that Rayleigh one; Rayleigh receivers are already available as ground instruments.

2. Mie receiver design and expected performances.

A Mie incoherent receiver mainly consists in a high resolution interferometer and a photon counting detector. Two high resolution interferometer could be envisaged: a Fabry-Pérot interferometer, which provides circular fringes whose radius is proportional to the square root of the spectral shift, and the Fizeau interferometer, which provides a linear fringe, whose position in the image plane is proportional to the spectral shift. Fringe imaging and energy measurement require detectors with c rcular geometry for the Fabry-Pérot type and bi-dimensional arrays detectors for the Fizeau type. However, both interferometers provide comparable spectral resolution.

The photon flux reaching the detector, once integrated over a time equivalent to 1 km altitude (8.3 µs), ranges between few tens of photons and 0.2 photon per each emitted laser pulse. The signal is increased by accumulation of several laser shots: assuming the specified cluster size (35 km) and a satellite velocity of 7 km/s, the available time-window (5 sec) allows to accumulate up to 500 laser shots. Due to the very low received flux and to the accumulation constraints, the detector has to provide real photon counting capability. Two are the types of detectors which meet this requirement, the Light Intensified CCD (LICCD) and the multi-anode MCP intensifier.

A LICCD is shown in figure 2/1: the light is first converted in photo-electrons by the photo-cathode, then intensified by Micro Channel Plates (MCP) and finally converted again in photon signal by a phosphor screen. In general the screen is coupled with the CCD array by means of a fibre optic taper.

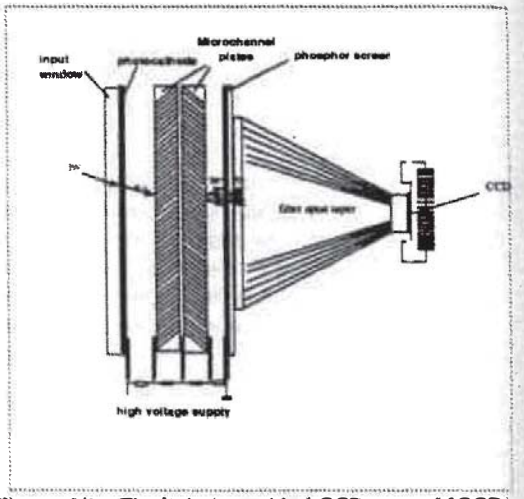

Figure 2/1 : *The light intensified CCD array(LICCD)*

For the LICCD, the photon counting operation is achieved, if the MCP gain noise is sufficiently low. Using a multiple stage intensifier allows to obtain a gain distribution of nearly gaussian shape, whose FWHM is about 80% of the mean gain. Analyses show that, under these conditions, the photon counting mode is nearly achieved. Another important design aspect is the CCD read-out sequence : being the temporal sampling 8.3 µs, the CCD array has to be clocked at a very high frequency and the CCD must be consequently as small as possible. For instance, if a 16*16 CCD is used, a

pixel rate of 30 MHz would be necessary to achieve a real-time image read-out . On the other hand, the CCD geometry is optimum for the coupling with a Fizeau interferometer, since the output fringe is linear and the fringe displacement is proportional to the spectral shift. When the fringe is aligned to the CCD, for example to the direction of the sensor columns, the spectral shift information is contained in only one dimension, i.e. the direction parallel to the fringe is of no interest. This feature can be employed to enhance the return signal, if the CCD is clocked using a specific timing sequence. Instead of reading all pixel of all lines every 8.32 µs, all lines of the CCD image zone are added within the first line of its memory zone. At the end of the laser echo sampling, the memory zone is then filled with N lines, each containing information related to one temporal sample. The dead time between two consecutive shots (10 ms) can then be used to read out the CCD memory zone. This principle allows to significantly decrease the pixel rate and then the detection chain criticality. This principle, which allows to directly retrieve the spectral shift versus time in the memory zone, is depicted in more detail in figure 2/2.

The second type of available photon-counting detector is the MCP intensifier coupled with a multi-anode focal plane. In this case, the phosphor screen and the CCD array are replaced by anodes, which directly detect the electron packets at the MCP output. Since many types of anode geometry is feasible, this solution is interesting to match the output beam of a Fabry-Pérot interferometer, where circular fringes are generated. A drawback resides in the need of multiple detection chains (as many as the number of anodes), which renders the electronic design more complex with respect to the LICCD, for which only one detection chain is needed.

On the other hand, the MCP gain noise may be suppressed by signal thresholding, but the counting rate

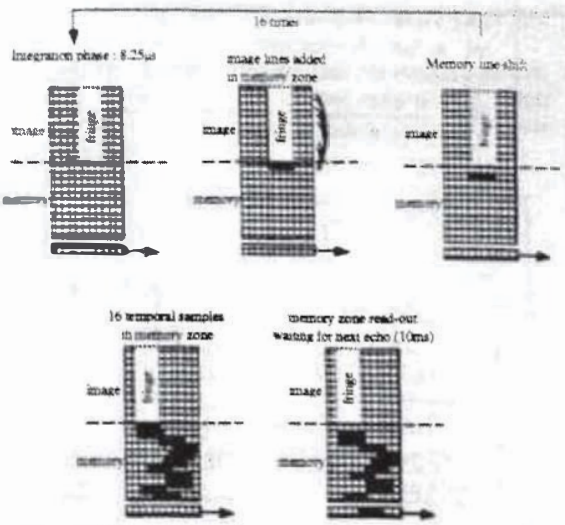

Figure 2/2 : CCD read-out principle (MMS patented) for a 16 x 16 pixel frame transfer CCD

capability is lower than for the LICCD.

In conclusion, two solutions seems to be of interest for a direct detection Mie receiver : a Fabry-Pérot interferometer coupled with multi-anode MCP intensifier and a Fizeau interferometer coupled with LICCD.

A trade-off of the two receiver concepts showed that both solutions give equivalent performance, but the Fabry-Pérot solution presents some drawbacks at instrument design level (as alignment constraints or flux dynamic limitation): the Fizeau solution seems actually to be more compact and robust than the Fabry-Pérot and it was proposed as a baseline for breadboarding. The proposed receiver concept, based on a Fizeau interferometer is shown in figure 2/3.

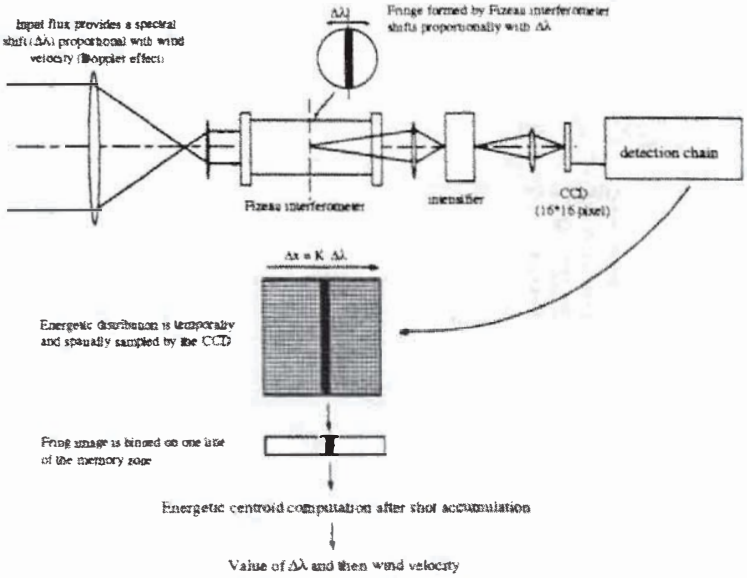

Figure 2/3 : *The receiver demonstrator is based on Fizeau interferometer with LICCD*

The Fizeau interferometer itself was early identified as an actual development challenge. Its performance specifications and derived design requirements are given in table 2/4 :

Performance parameter	Value
Operating wavelength	354.7 nm
Finesse	> 15
Peak transmission	> 0.7
Dispersion	12 fm/mm
Free spectral range	0.4 pm
Useful diameter	28 mm
Design parameters	
Spacing between etalon	157.3 mm
Wedge angle (a)	5.37 µrad
Etalon plate reflectivity	0.85
Etalon plate spherical bowing	< λ/100
Etalon plate roughness	< 10 Å rms.

Table 2/4 : *Fizeau performance and design parameters*

The specified finesse is equivalent to a spectral resolution of about 26 fm at FWHM. The design parameters are optimised, taking into account the different contributions to the finesse: reflectivity, plate bowing, roughness, effect of input beam divergence and wedge angle. The main challenge in designing and manufacturing the interferometer is its spectral stability. When operating at ambient laboratory conditions, the first effect to suppress is the air index variation versus temperature and pressure. This problem was solved choosing an hermetically sealed interferometer: in this case, assuming that the interferometer contains a perfect gas, being the ratio P/T constant, the refractive index shall also be constant. The drawback of this solution is that changes of external conditions may generate mechanical perturbations on the etalon plates and then induce bowing. This problem was solved, as depicted in figure 2/5, using counter-plates which ensure pressure equilibrium on both sides of the etalon, whatever the external pressure and/or the temperature. Another effect to be compensated is the expansion of the spacers between etalon plates due to temperature variations, which has a dramatic effect on the stability of the output fringe. This was solved using Zerodur spacers whose Coefficient of Thermal Expansion (CTE) is chosen to match and compensate the other effects. The overall CTE between etalon plates was then estimated around 0.8 10^{-9}/°C. This means that the distance between etalon is stable to about 1 Å/°C. The etalon plates are of fused silica: the differential CTE between Zerodur and silica is compensated by dilatation grooves. The interferometer is totally assembled using molecular bonding : this space qualified technology prevents from stability problems frequently encountered when using classical glue bonding. The adopted reflective coating was also subject to careful trade-off, since hard coating may disturb the initial etalon plate flamess due to the surface constraints they involve once deposited. On the other hand, hard coatings are simpler to realise and to apply. Eventually, soft coatings were chosen and their optimisation needed several trials.

The Fizeau interferometer was realised by STIGMA-OPTIQUE (France), which anticipated the manufacturing phase by preliminary mechanical validation in order to assess the proposed design. The final interferometer tests assessed its initial performance parameters. The finesse was checked to be 15.4 and the dispersion and the thermal stability was measured to be better than 0.25 fm/°C, what is equivalent to a spectral shift of 0.6 MHz/°C or 0.2 (m/s)/°C, (on horizontal wind with 36° slant angle). The dispersion at the interferometer output was verified to be 11.8 fm/mm what is very close to the specified value.

The success in designing and manufacturing the Fizeau interferometer was a major achievement in the programme progress and receiver performance tests confirmed the quality of the device.

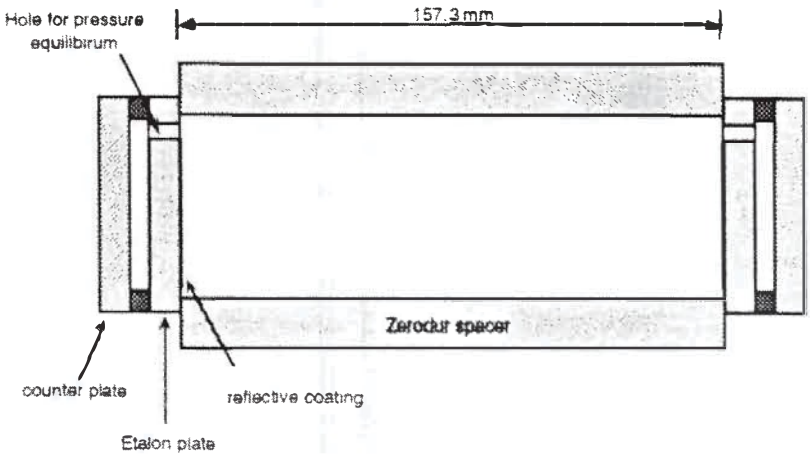

Figure 2/5 : *Fizeau interferometer design*

As mentioned before, the detection package is based on a light-intensified CCD array, whose read-out sequence is optimised for operation with a Fizeau interferometer. The CCD array is a THOMSON product (TH31160) which was developed for the SILEX programme (inter-satellite laser communication experiment). This space-qualified device is a frame-transfer detector with 16*16 pixel of 23 µm pitch. A high line-rate operation is possible due to its small size, as confirmed by the initial application in SILEX programme. This feature is of paramount importance since the line transfer duration - when binning the image zone in the memory zone - determines the cross-correlation between temporal samples. A line rate of 12.5 MHz was applied without degradation of the transfer efficiency and with a cross-correlation between temporal samples lower than 2 %.

The post-detection electronics consists in a conventional 12 bit digitisation unit, whose dynamic is adjusted to the full-well capacity of the CCD. The low pixel rate (100 kpixel/s) needed when using the specific read-out sequence allows to significantly decrease the criticality of this electronic chain.

The optical coupling between the intensifier output and the CCD array is realised with two microscope objectives which allow to reduce the size of the image available at intensifier output. Although the reduction factor (4.5) may be also reached with a fibre optic taper, discrete optics solution was chosen in order to allow magnification adjustment during the development phase.

The intensifier is a custom design from PHOTEK (UK). Due to the small size of the image at intensifier input, the MCP stages have been chosen of high spatial resolution (pore of 6 µm diameter). Note that the small pore diameter also allows to reduce the pile-up effect. The photo-cathode material is a bi-alkali in order to optimise the quantum efficiency at the UV wavelengths. The choice of the phosphor required a careful trade-off. As a matter of fact, the phosphor decay time is of major importance when analysing the cross correlation between temporal samples. Being the sampling period about 8.3 µs, the phosphor decay time has to be much lower to ensure that one given temporal sample is not disturbed by the previous ones. On the other hand, lower decay times are obtained with blue emitting phosphor, but these are not compatible with the CCD spectral sensitivity. Finally, a compromise solution was found to be the P46 phosphor, whose emission spectrum is comprised between 500 and 650 nm, and whose decay time at 10% is lower than 150 ns.

The intensifier performance, as measured by the manufacturer and experimentally assessed at MMS, are given in table 2/6. The detection quantum efficiency (DQE), which is the equivalent efficiency once the pore filling factor is taken into account, is about 15%, a rather high value with respect to standard results obtained at 355 nm. The dark count rate is higher than initially expected (20 count/s/cm²), but this has no impact on the receiver performance, due to the very short integration time (8.3 µs) and the small image size (2.6 mm²).

The photon gain is high enough to require special precaution when switching on the intensifier. The test bench was optimised in order to limit as far as possible the stray-light.

Parameter	Validated value
Photo cathode quantum efficiency at 355 nm	0.276
Dark count rate at 20°C	*180 c/s/cm²*
Number of stage	2
L/D ratio	80:1
Pore diameter	6
Pore spacing	7.5
Pore filling factor	0.57
Recovery time	< 9 ms
Photon gain	$1.25\ 10^6$ ph/ph
Pulse height distribution	*0.8*
Spatial resolution (FWHM)	36 µm
Phosphor decay time (90%-10%)	< 0.2 µs
Useful diameter	12

Table 2/6 : *Intensifier actual performances.*

The pore recovery time was chosen to be lower than the laser shot period in order to minimise the pile-up effect : when a given pore amplifies a photo electron, 9 ms are necessary to recover its full ability to amplify. An excessive recovery time involves a decrease in the apparent intensifier gain for a given input flux.

The spatial resolution of the intensifier which involves not only the pore diameter but also the phosphor gain is equivalent to 8 µm at CCD level, which is much lower than the pixel size.

Once assembled, the intensified detection chain provides the following performance:

- Detection chain gain : 38 LSB/photon or 250 LSB/count. The CCD chain noise in darkness (1.4 LSB/pixel) is negligible with regard to this gain.
- Linearity error : lower than 1 % on the useful signal dynamic.
- Quantum efficiency at 355 nm : 15%.

3. The Laser Signal Simulator (LSS).

The LSS is the optical signal source which simulates the Lidar return pulses. The LSS can operate in a so-called long-pulse mode (a 130 µs modulated pulse which simulates the lidar return signal), but also in CW and in a so-called short-pulse mode (10-20 ns pulses), which have been used for alignment, calibration and test of the receiver demonstrator. To simulate both Rayleigh and Mie signals, the LSS provides a narrow spectral bandwidth laser beam with precisely controlled frequency and amplitude, superposed to an incoherent wide-bandwidth (20-30 nm) background radiation. For the Mie signal (i.e.: laser), a frequency modulation with a maximum excursion of 400 MHz, a maximal sweep

speed of 2 MHz/µs and a synchronised amplitude modulation with high extinction ratio are also required. For easy and reproducible interfacing of the LSS with the receiver demonstrator, a fibre delivery with a 50 µm core fibre is implemented. The figure 3/1 shows the optical layout of the LSS.

To satisfy the very stringent frequency and amplitude stability requirements of the LSS, a dual wavelength laser source (Lightwave Electronics LT 142) has been selected. To guarantee a sufficient long term (10 hours) frequency and amplitude stability, the whole laser is temperature stabilised in an isothermal box to less than 0.01°C temperature variations. Both output beams of the LT 142 are overlapped with the correct polarisation at the common focal point, in a 15 mm long LBO crystal, for the type-II frequency tripling. This crystal is temperature-stabilised to maintain high amplitude stability during the third harmonic generation. Actually lidar return pulse simulation requires only very low radiometric levels (typically less than 0.1 nW) and so, the optimisation of non-linear conversion efficiency did not represent a serious problem. Frequency modulation of the 355 nm laser beam is performed by two acousto-optic frequency shifters (AOM), in a four pass, forth-back configuration, to fulfil simultaneously the required large frequency excursion and the beam pointing stability at the output (necessary for the subsequent fibre delivery). The amplitude control is performed with a low-voltage transverse-field electro-optic modulator (EOM). The incoherent wide-band radiation required for the background is provided by a DUV-35W (Philips) Xenon arc lamp, with appropriate filtering. To control the amplitude of the incoherent background flux, an electrically-steerable liquid crystal half-wave plate is introduced in the optical path. Mixing of laser and background light beams, both linearly polarised, is efficiently implemented by a polarising beam-splitter cube. The electronic drivers of the amplitude and frequency modulators are driven by a PC-programmable 50 MHz dual-channel arbitrary wave-form generator which allows a very easy and flexible simultaneous control of the frequency and of the amplitude of the laser radiation.

The frequency stability of the 355 nm output, measured by comparison with the MMS Fizeau interferometer, showed peak-to-peak deviations of maximum 18 MHz. Under the assumption of Gaussian noise and a ± 3σ interval for the peak-to-peak deviations, this value corresponds to a standard deviation of σ = 3MHz. This value represents the mutual stability of the laser and the Fizeau interferometer. The maximum laser output flux at 355 nm, with the AOM's in the 0th order, was measured at 35 nW. In the 1st order of the AOM's, for a total frequency shift between 480 and 720 MHz, the output is of the order of 1.25 nW. Being the diffraction efficiency of the AOM's highly frequency-dependent, the output flux during a frequency scan is not constant. However, as far as the amplitude and frequency can be controlled by the (software programmable) arbitrary wave generator, it is possible to generate a compensating amplitude transmission function. This was implemented by generating a linear amplitude ramp, synchronised with the corresponding linear frequency ramp. The on-off contrast of the EOM resulted to be another critical issue and a maximum contrast of 560 could be obtained, against the original specification of 10^5.

As the output fibre is multi-mode for the 355 nm radiation, the output intensity distribution is affected by speckles of a mean diameter depending on the exact injection conditions. Anyway, the averaged output intensity distribution measured after shot accumulation was nearly a flat-top. The verification test sequence of the LSS confirmed the initial predictions and expectations: although some aspects were not compliant, the LSS provided sufficiently high performance to realise reliable and reproducible tests on the receiver demonstrator.

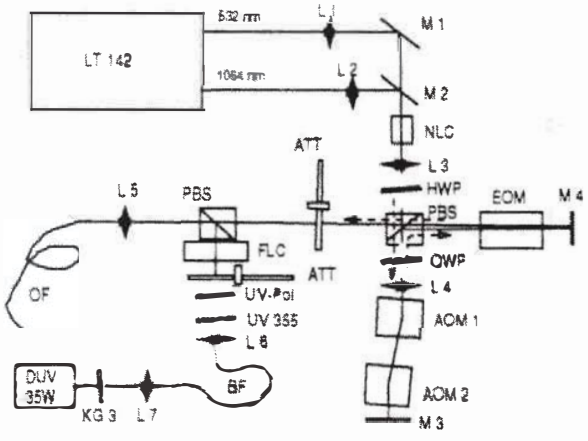

Figure 3/1 : *LSS optical layout*

LT 142	Dual wavelength single longitudinal mode laser (Lightwave Technology)
NLC	Non linear, frequency tripling crystal (type II LBO).
EOM	Electro-optic intensity modulator.
AOM	Acousto-optic frequency modulators.
DUV35W	Xenon arc lamp.
OF	Output fibre (50 µm, ON=0.22)
L1,	Focusing lens, 532nm
L2	Focusing lens, 1064nm
L3	Collimating lens, 355nm
L4	Focusing lens for AOM's, 355nm
L5	Fibre injection objective, 355nm
L6	Arc lamp collimating lens, 355nm
L7	Arc lamp fibre injection, 355nm
M1	Mirror, 532nm, 45°
M2	Mirror, HR 1064nm, HT 532nm,
M3, M4	Mirror, HR 355nm, HT 532nm/1064nm
PBS	Polarising beam splitter
HWP	Half wave plate, 355nm
QWP	Quarter wave plate, 355nm
ATT	Attenuation filters
IF	Filter 355nm

4. Receiver performance test summary.

The validation approach for the receiver performance consisted in creating a performance simulation software, in validating its results by specific tests performed on the breadboarded demonstrator, and finally in using it to derive the expected performances versus altitude.
Optical transmission, linearity, spectral transfer function, memory effects and other stand-alone device performance were tested on the demonstrator, in order to verify the assumptions; however, only main performance test results will be reported in the following.

4.1 - Signal to Noise ratio

The knowledge of the Signal to Noise Ratio (SNR) allows to assess whether the intensified detection chain actually works in photon-counting mode. In this case, the SNR curve should be the "pure" square root of the detected photons (i.e.: counts). Figure 4.1/1 gives the measured SNR for a signal comprised between 0.05 and 1.9 photon/acquisition (on this figure the signal is given in LSB at detection chain output, the gain being 38 LSB/photon). The measured SNR fits a square root function of the incoming signal for very low input flux : this confirms that the detection chain actually works in photon-counting mode. As a matter of fact, detection chain whose performance are limited by their noise in darkness, provide SNR curve that is proportional with the signal at very low input flux.
The measured SNR curve also shows a deviation from the expected profile, at higher input fluxes : this means that the detection gain is lower than expected. This gain loss effect is probably due to the pile up effect.

4.2 - Derived performances versus altitude.

Performance tests were performed on the receiver demonstrator, simulating the radiometric conditions of the ARMA atmosphere model, used for the ESA ATLID programme [3]. The Mie and Rayleigh fluxes were simulated by the LSS for an equivalent altitude comprised between 1 and 7 km. This allowed to verify whether the simulation software provided reliable results. During these tests, it appeared that the performances were actually reached for a Mie flux twice higher than initially foreseen by the simulation software. Since the Mie flux doubles every altitude kilometre, this results implies that the maximum operating altitude for a given false alarm rate is one kilometre lower than initially expected.
Note that the occurrence of this performance discrepancy is mentioned in the literature also for coherent lidar receivers: in fact, it is reported that the actual performance of a coherent receiver are obtained with a SNR impairment ranging from 3 to 8 dB [4].
Once the simulation software was up-dated to take into account this discrepancy, the actual demonstrator parameters, notably the measured Fizeau and intensifier performance, were fed into the simulation software to derive the wind-measuring performance versus altitude. The results are shown in figures 4.2/1 and 4.2/2.
Figure 4.2/1 compares the measurement noise that was expected during the study phase ("initial") and the noise actually measured ("final"), assuming instrument design assumptions, as proposed in table 1.2.

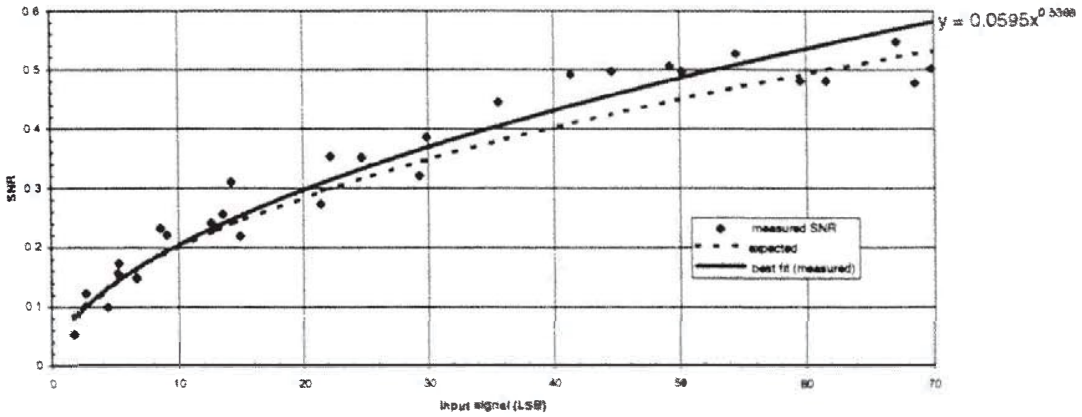

Figure 4.1.1/1 : *Comparison between measured and expected SNR.*

The noise is computed on both "good" acquisitions (Pd) and false alarms (Pfa). The false alarms are here defined as the measurements whose error is higher than 10 m/s (i.e.: one pixel), and which are not filtered by the post-processing algorithm. This one consists in comparing the Mie signal level with a threshold defined as a function of the estimated Rayleigh background. As mentioned before, in figure 4.2/1 a 1-km altitude shift between initial and final predictions is appearing. Note that the altitude is given as a vertical projection and that the noise is given for horizontal winds, assuming emission is performed with 36 ° slant angle. Note also that these performances were obtained with a horizontal wind dynamic of ± 43 m/s, which is compatible to the specified operation range from 0 to 10 km altitude.

Figure 4.2/2 compares the initial and final expectations for characteristic probabilities. These are :

- detection probability (Pd) : probability to detect the Mie spike signal over Rayleigh background with an accuracy better than 10 m/s (maximum allowed error for a good detection).
- false alarm probability (Pfa) : probability that one acquisition is declared "good", although the error is higher than 10 m/s. This is the percent of aberrant acquisitions that could not be filtered by the post processing.
- Non detection probability (Pnd) : probability that one acquisition is rejected by the post processing.

Figure 4.2/1 : *Evolution between initial estimation and final one for a flight instrument*

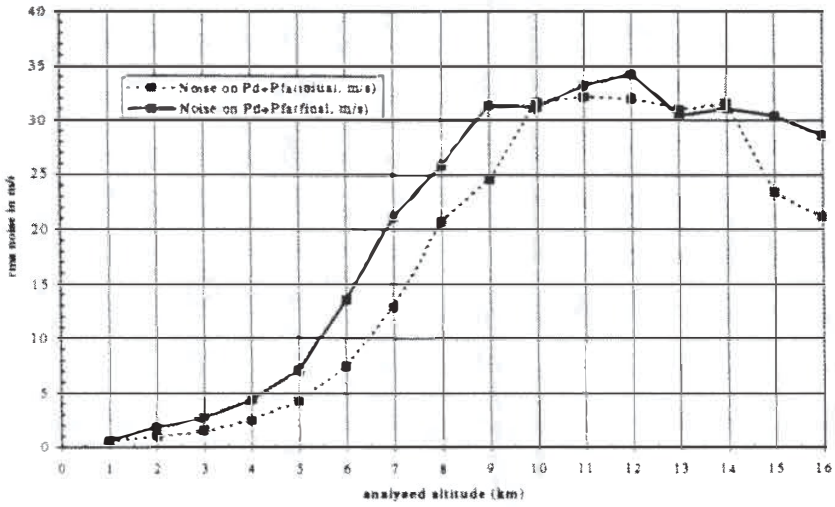

Figure 4.2/2 : *Probability Evolution between initial and final estimations for a flight instrument*

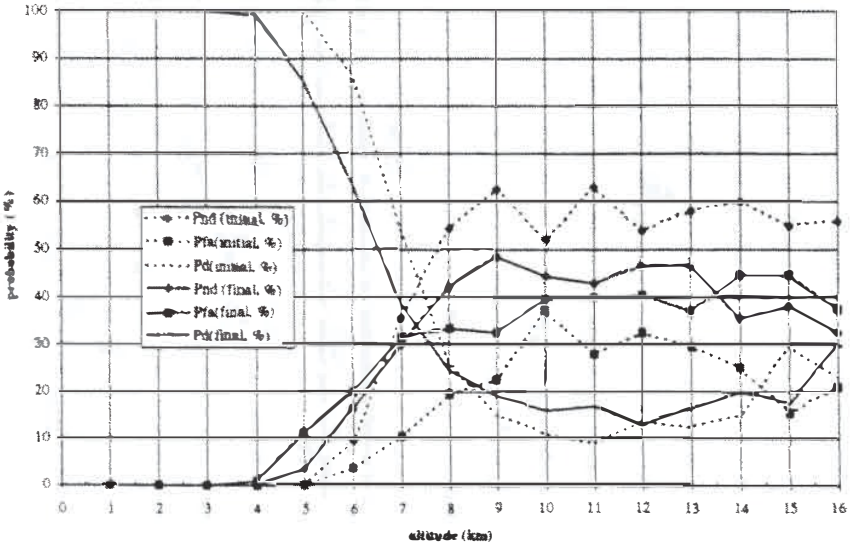

Figure 4.2/2 shows that the detection probability remains higher than 80% up to 5 - 6 km, and that the false alarm rate remains lower than 20% up to 6 km. This means that, with instrument and mission requirements proposed in tables 1/1 and 1.2, the Mie receiver can provide reliable measurements up to 5 - 6 km. Within this altitude range, the measurement accuracy, i.e. the rms. noise, is comprised between 0.5 and 8 m/s on horizontal winds (36° slant angle), which is equivalent to a LOS wind rms. error comprised between 0.3 - 4.5 m/s

4.3 - Receiver spectral transfer function.

The receiver spectral transfer function characterises the measurement linearity on the total receiver dynamic range, including interferometer and post processing effects. The receiver was designed to provide a linear transfer function versus input spectral drift, and the slope is expected to be about 35 MHz per CCD pixel (or 10 m/s per pixel). The measured transfer function is given in figure 4.3/1.
The linear interpolation of the measured points gives a spectral dispersion of about 34.5 MHz/pixel, which is very close to the expected value. The overshoots with respect to the ideal line are due to local defects on the Fizeau interferometer, which enlarge the fringe for a given spectral shift and then generate truncation effects in the centroiding process. This phenomenon may be suppressed either improving the Fizeau etalon plate flatness or calibrating the linearity error. Figure 4.3/1 also demonstrates that the receiver spectral dynamic range is about 290 MHz, which is equivalent to ± 43 m/s horizontal wind.

4.4 - Interferometer thermal stability.

The thermal stability of the interferometer is, as already mentioned in the previous paragraph, one of the major challenges of this study. As a matter of fact, the interferometer sensitivity to its thermal environment determines the criticality of the thermal control to be implemented in the flight instrument. The preliminary development phases for the Fizeau interferometer allowed to define a high thermal stability design. These properties were experimentally checked at MMS and confirmed the high thermal stability of the optical path difference: the equivalent CTE was estimated to be about 0.6 10^{-6} /°C, confirming the design values. The distance between etalon plate remains constant to better than 1 Å for 1°C temperature change.
On the other hand, it appeared during thermal tests that the dispersion (i.e.: the tilt angle between etalon plates) was sensitive to the transverse thermal gradient. Main consequences on the design of a flight unit are that the transverse thermal gradient control is more critical than the absolute temperature control: 1°C temperature drift is acceptable although transverse thermal gradient should remain below 0.1°C. Still, the control of the detection package to such a degree of thermal stability should not represent a matter of concern for the design of the space-borne unit.

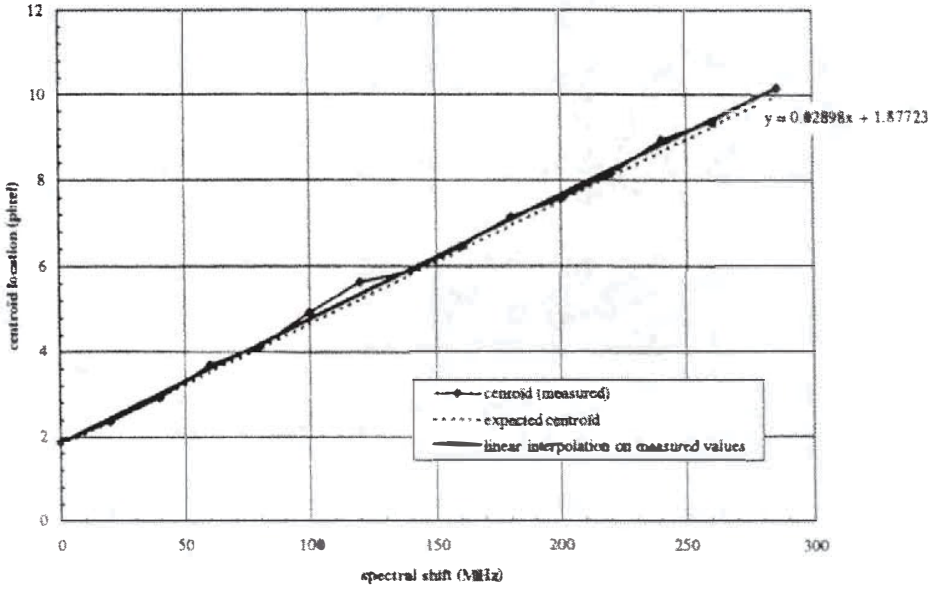

Figure 4.3/1 : *receiver spectral transfer function*

5. Conclusions.

The results of the "IDWL technologies" study, demonstrated that the concept initially proposed by MMS, based on a Fizeau interferometer coupled to a light-intensified CCD array, meets the specifications and the expected performance. The projected capability of the Mie receiver would permit to perform wind measurements with the required accuracy and with low false alarm rate up to 5 - 6 km altitude. The technology has been proven to be robust and simple enough to consider future space qualification without major reasons of concern. Therefore, it is reasonable to predict that this IDWL concept is suitable to be developed into a performing flight-unit, for wind measurements with high accuracy in the first 5 km of the atmosphere. Indeed, comparing prospected performance of lidars based on coherent and incoherent detection techniques and considering the inherent simplicity of the incoherent detection techniques and instrument concept, IDWL demonstrates to have a high potential and can be considered a valuable alternative to coherent Doppler wind lidar instruments for a satellite-based global wind sensing system.

6. Acknowledgements

This work has been funded by the European Space Agency, under Work Order 15, ESA Contract 9777/92/NL/PB.

7. References

1. "Atmospheric Dynamics Mission", Report for assessment of the nine candidate Earth Explorer missions, No.4 - ESA Publications SP-1196(4), April 1996
2. U.Johann, F.Safa et al.: "ALADIN: mission and instrument concept of an European spaceborne CO_2 laser Doppler wind lidar" in Proc. of 8th Coherent Laser Radar Conference, Keystone - CO (USA) July 1995.
3. D.Morancais, A.Marini: "Atmospheric lidar pre-development programme (ATLID)" . Proc. SPIE Vol. 3117, SPIE 42nd Annual Meeting, S.Diego - CA (USA), July 1997.
4. RM Gagliardi, S. Karp : "Optical communication" Springer-Verlag

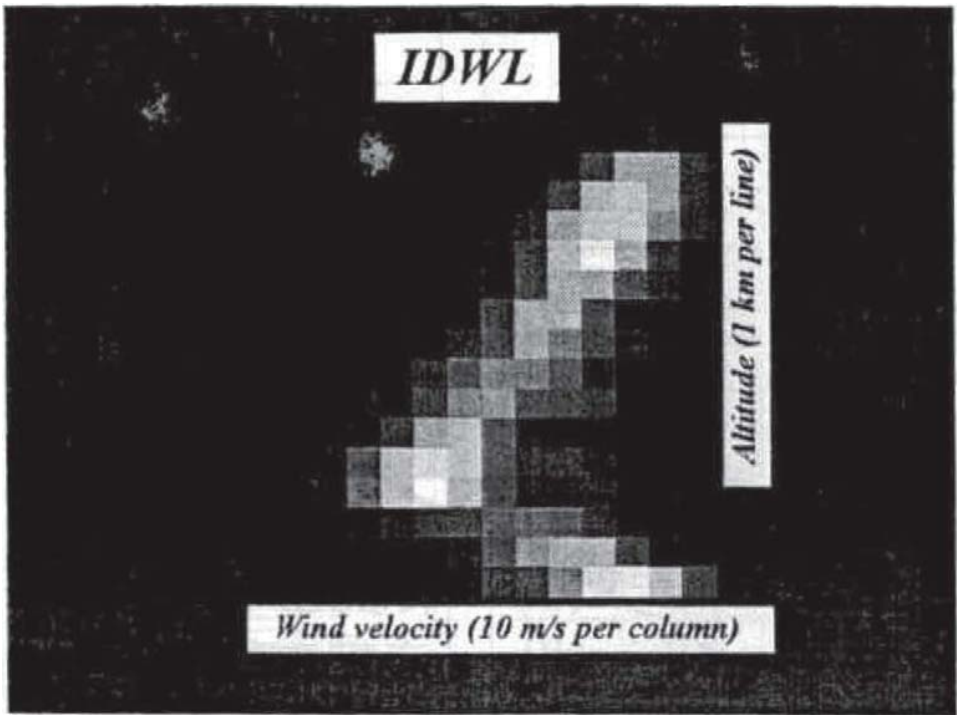

Analogue acquisition obtained with double slope frequency modulation (0 -> 80 m/s)